Scripta Materialia 237 (2023) 115687

Contents lists available at ScienceDirect

Scripta Materialia

journal homepage: www.journals.elsevier.com/scripta-materialia

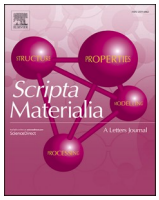

Elastic strain associated with irradiation-induced defects in self-ion irradiated tungsten

Guanze He [a], Hongbing Yu [b,*], Phani Karamched [c], Junliang Liu [c], Felix Hofmann [a,*]

[a] Department of Engineering Science, University of Oxford, Parks Road, Oxford OX1 3PJ, UK
[b] Canadian Nuclear Laboratories, 286 Plant Road, Chalk River, ON K0J 1J0, Canada
[c] Department of Materials, University of Oxford, Parks Road, Oxford OX1 3PH, UK

ARTICLE INFO

Keywords:
HR-TKD
TEM
Tungsten
Dislocation loop
Elastic strain
Irradiation damage

ABSTRACT

Elastic interactions play an important role in controlling irradiation damage evolution, but remain largely unexplored experimentally. Using transmission electron microscopy (TEM) and high-resolution on-axis transmission Kikuchi diffraction (HR-TKD), we correlate the evolution of irradiation-induced damage structures and the associated lattice strains in self-ion irradiated pure tungsten. TEM reveals different dislocation loop structures as a function of sample thickness, suggesting that free surfaces limit the formation of extended defect structures that are found in thicker samples. HR-TKD strain analysis shows the formation of crystallographically-orientated long-range strain fluctuations above 0.01 dpa and a decrease of total elastic energy above 0.1 dpa.

Introduction

Irradiation-induced lattice defects in crystalline materials are key to understanding in-reactor property degradation of nuclear materials. These lattice defects span a wide range of sizes, and several different types can be distinguished, such as point defects, defect clusters, dislocation loops and voids. Dislocation loops have received the most attention, because they can be readily observed by transmission electron microscopy (TEM), and are formed in different nuclear materials [1,2].

TEM studies of the evolution of dislocation loop structures under different irradiation conditions, e.g. temperature, irradiation species, and irradiation dose rate, are essential for understanding defect accumulation. They provide a pathway for predicting the evolution of irradiation-induced damage in structural materials exposed to reactor environments [3] and enable validation of irradiation damage simulations [4–6]. Previous TEM studies of irradiation-induced dislocation loops have primarily focused on microstructural features, such as loop size, density, morphology, Burgers vector, nature, distribution and elemental segregation [7–10].

Elastic strain fields due to irradiation defects remain largely unexplored. Yet elastic interactions play a critical role in controlling dislocation loop morphology, evolution and the formation of self-organised dislocation structures [11,12]. This effect is particularly important at damage doses >0.1 displacement per atom (dpa) [12]. Experimentally, there are limited options for probing elastic strain fields associated with irradiation defects, though a few exploratory studies have been carried out: Longer range (μm scale) strain fields have been non-invasively probed, with depth resolution, using synchrotron X-ray micro-Laue diffraction [13–15]. Multi-reflection Bragg coherent X-ray diffraction imaging (MBCDI) has been used to characterise elastic strain fields of ion-irradiation-induced defects with higher (~30 nm) 3D spatial resolution [16–18]. In self-ion-irradiated tungsten this revealed large nano-scale fluctuations of lattice strain [17]. However, MBCDI is limited in spatial resolution, requires difficult sample preparation and synchrotron access.

Cross-correlation-based high angular resolution electron backscattered diffraction (HR-EBSD) offers a precise, rapid, and non-destructive tool for measuring strain on sample surfaces [19]. In self-ion-irradiated tungsten it revealed long-range (beyond the length scale of the strain field of an isolated dislocation loop) strain fluctuations at 1 dpa due to defect self-organization, but failed to probe short-range (on the order of the length-scale of the strain field of an isolated dislocation loop) lattice distortions at lower doses ($\leq$ 0.01 dpa) due to limited spatial resolution [20]. High resolution transmission Kikuchi diffraction (HR-TKD) offers much higher spatial resolution (5–10 nm) [21–23] and enables measurements of strain fields of individual isolated dislocations [24]. Here we report the use of HR-TKD to probe the evolution of elastic strain fields caused by irradiation-induced defects from low to high

* Corresponding authors.
E-mail addresses: hongbing.yu@cnl.ca (H. Yu), felix.hofmann@eng.ox.ac.uk (F. Hofmann).

https://doi.org/10.1016/j.scriptamat.2023.115687
Received 23 November 2022; Received in revised form 25 July 2023; Accepted 26 July 2023
Available online 2 August 2023

doses. TEM is used to image the defect structures for a direct comparison. This prototypical study focuses on pure tungsten, the main candidate for plasma-facing fusion reactor armour [25,26].

Experimental method

High purity polycrystalline Tungsten (99.99 wt%) foil (120 μm thick) was punched to 3 mm discs and annealed at 1200 °C for 24 h in vacuum. The discs were mechanically polished, and then twin-jet electropolished (0.5 wt% NaOH aqueous solution, 0 °C, 14 V) to make standard 3 mm TEM samples. These were irradiated at the Helsinki Accelerator Laboratory with 2 MeV $^{184}W^{2+}$ ions under a vacuum of 8 $\times 10^{-7}$ mbar at room temperature to doses of 0.01, 0.1, and 1 dpa. The beam current was calibrated by a Faraday cup and maintained at 7 - 8 nA/cm^2.The anticipated average displacement damage in the top 100 nm was estimated using the Stopping and Range of Ions in Matter (SRIM) code [27] (K-P calculation, threshold energy of 68 eV [15]). A fluence of 1.51 $\times 10^{14}$ ions/cm^2 was implanted to produce 1 dpa nominal damage in 123 min, corresponding to a damage rate of 1.36 $\times 10^{-4}$ dpa/s.

Dislocation loops were imaged using two-beam bright field (BF) and weak beam dark field (WBDF) imaging on a Jeol-2100 TEM (200 kV, LaB6 source). All images were taken under $g = 002$, $z = [001]$ diffraction condition. For each sample, regions with different thicknesses were imaged, and the local thickness in each region was measured by Electron Energy Loss Spectroscopy (EELS) using t/λ method on a Jeol ARM 200F microscope with a Gatan GIF Quantum 965 ER.

HR-TKD measurements were performed on a Zeiss Merlin SEM with a Bruker e-flash high-resolution EBSD and OPTIMUS™ TKD head. On-axis TKD configuration was used, i.e. the optical axis of the SEM intersects the centre of the phosphor screen, with diffraction patterns collected beneath the sample. This yields the strongest diffraction signals and minimises gnomonic distortions [28]. HR-TKD analysis focussed on [001] orientated grains using the following SEM operating parameters: 30 kV, 3 nA, 800 × 600 TKD pattern size, 5 mm working distance, 8 nm step size. Cross-correlation analysis of Kikuchi patterns was performed using the CrossCourt 4 software, with the saturated central region of the patterns excluded from analysis, as shown in supplementary figure S1.

Results and discussion

TEM observations of the morphology and distribution of dislocation loops in tungsten irradiated to different doses are shown in Fig. 1. The kinematic bright field images indicate that defect clustering (~ tens of nm length scale) depends on both the irradiation dose and the thickness of the sample. In the thin regions, dislocation loops appear to be isolated spots at all dose levels. The average size and number density of these loops grows with increasing irradiation dose. In the medium thickness regions, defects remain isolated spots in the 0.01 dpa sample, while some extent of defect clustering (also known as 'rafting' [7]) is observed in the 0.1 dpa sample. This is even more pronounced in the 1 dpa sample. In the thick regions, clustering of defects is visible at all dose levels from 0.01 to 1 dpa. This clustering is more prominent in bright field images, while the dark field images (contrast inverted in Fig. 1, original contrast images shown in supplementary Fig. S2) show isolated dot-like dislocation loops with some ordering. Compared to the kinematic bright field images, the contrast in the weak beam dark field images arises from the large lattice distortion close to the core of the dislocation loops [1], thus highlighting small dislocation loops.

The length scale of defect clustering visible in Fig. 1 can be quantitatively revealed by applying tangential integration to the 2D Fourier Transformation (TIFT) of the TEM bright field images (Fig. 2). For details of the TIFT method please refer to [20,29]. A characteristic length can be determined as the inverse of the spatial frequency at the peak position. For instance, the peak positions of the profiles for the 0.01 dpa, 0.1 dpa and 1 dpa sample thin regions are 1.2×10^{-1}, 7×10^{-2}, and 5×10^{-2} 1/nm, respectively. In real space, these correspond to characteristic length scales of 8.3 nm, 14.3 nm and 20 nm. Similarly, the characteristic lengths of the defect contrast at the medium region are 20 nm, 20 nm, and 40 nm from 0.01 dpa to 1 dpa. For the thick regions, they are 33.3 nm, 55.6 nm, and 125 nm respectively. TEM image intensity fluctuation arises from two main sources, one is from the individual dislocation loops, and the other is the clustering of defects. Individual defects

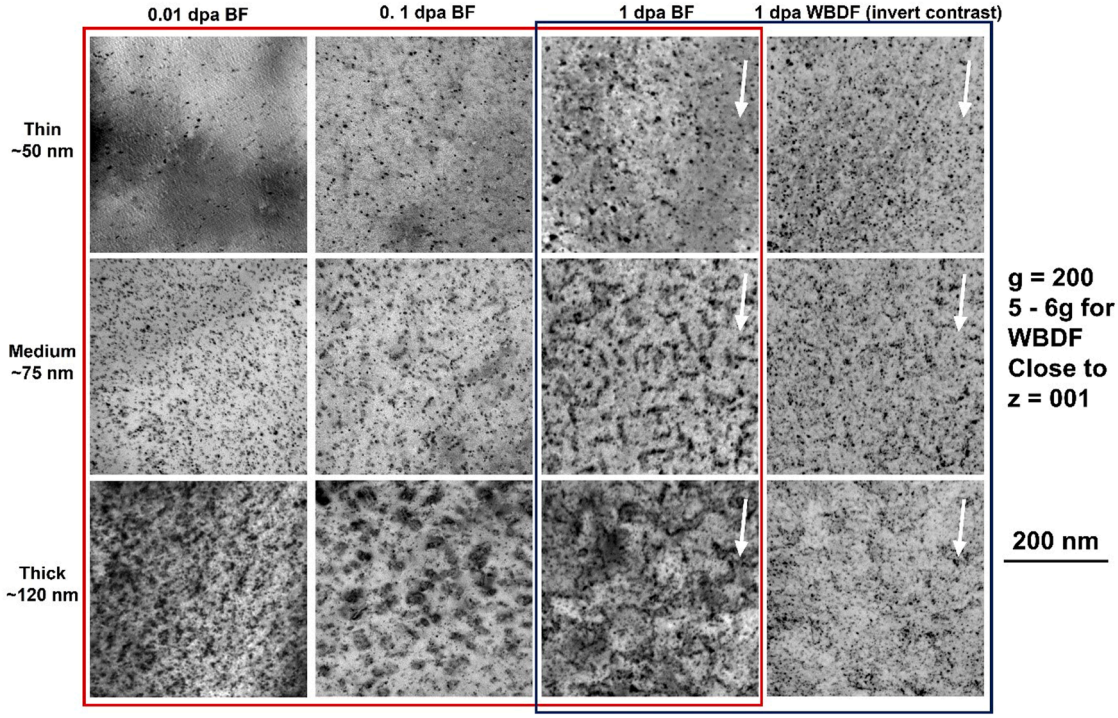

Fig. 1. TEM bright field images of the tungsten samples irradiated to 0.01, 0.1 and 1 dpa. In each sample, images were taken from thin, medium and thick regions of the same grain (see supplementary Fig. S3). For the 1 dpa sample, weak beam dark field images were also recorded at the same positions as the bright field images.

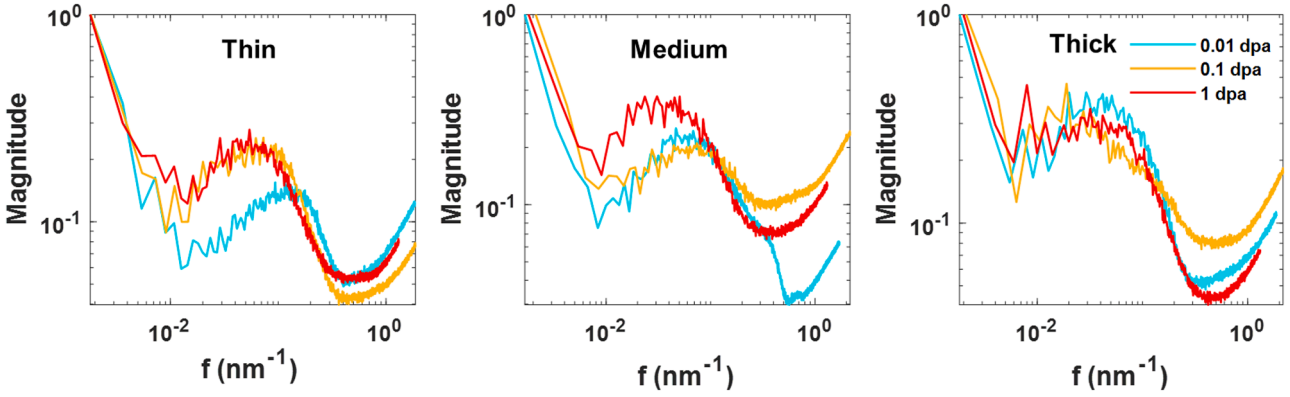

Fig. 2. Tangential integration profiles of the 2D FT of the TEM bright field images (TIFT analysis). The magnitude is normalized to 1 at zero frequency.

are small, contributing to high-frequency signals in the FFT profile, while clustering contributes to lower-frequency signals. As such, the peak in the FFT profile reflects the size of the defects' extended strain field if they are isolated (thin regions) or the scale of defect clustering if clustering dominates (medium and thick regions). These results suggest that the length scale of the defect contrast fluctuations increases with both dose and thickness. At the same dose level, defect clustering is more prominent in thicker samples, presumably due to a reduced effect of the free surfaces. Previous work showed that dislocation loops are attracted to free surfaces, resulting in an underestimate of dislocation loop density in TEM images [30]. The TIFT analysis shows that free surface can also limit multi-body interactions of defects and thus prevent the formation of longer-range structures. At the same thickness (except for the thinnest regions) the extent of defect clustering increases with the dose level.

To explore the driving force behind the self-organization of dislocation loops, HR-TKD was used to map the 2D elastic strain fields associated with the irradiation-induced defect structures in the 0.01, 0.1 and 1 dpa samples. HR-TKD measurements in all samples were performed in the medium thickness regions (see Fig. S3), which yielded the best Kikuchi patterns. For each sample, TKD was performed on the same grain where TEM images in Fig. 1 were recorded, but not at the exactly same location due to experimental difficulties in doing so. For the grains selected in the 0.01, 0.1 and 1 dpa samples, the misorientations between the [001] direction and the surface normal were 22.4°, 23.7° and 5.6° respectively. Since the defect structures may vary with surface orientation [7], the grains should ideally have the same out-of-plane orientation. However, the choice of grains is limited in practice, and grain morphology (size, thickness, bending or not etc.) must be considered. The above misorientations are thus the best we could achieve. HR-TKD measures deviatoric strain, reflecting the angular distortion of lattice planes, as cross-correlation based EBSD or TKD analysis is not sensitive to lattice dilations [19]. Because there is no strain-free reference point available in the irradiated samples, the deviatoric strains measured in the irradiated samples are relative values to the arbitrarily selected reference point with the best diffraction pattern quality. As such, these strain field maps reflect the spatial

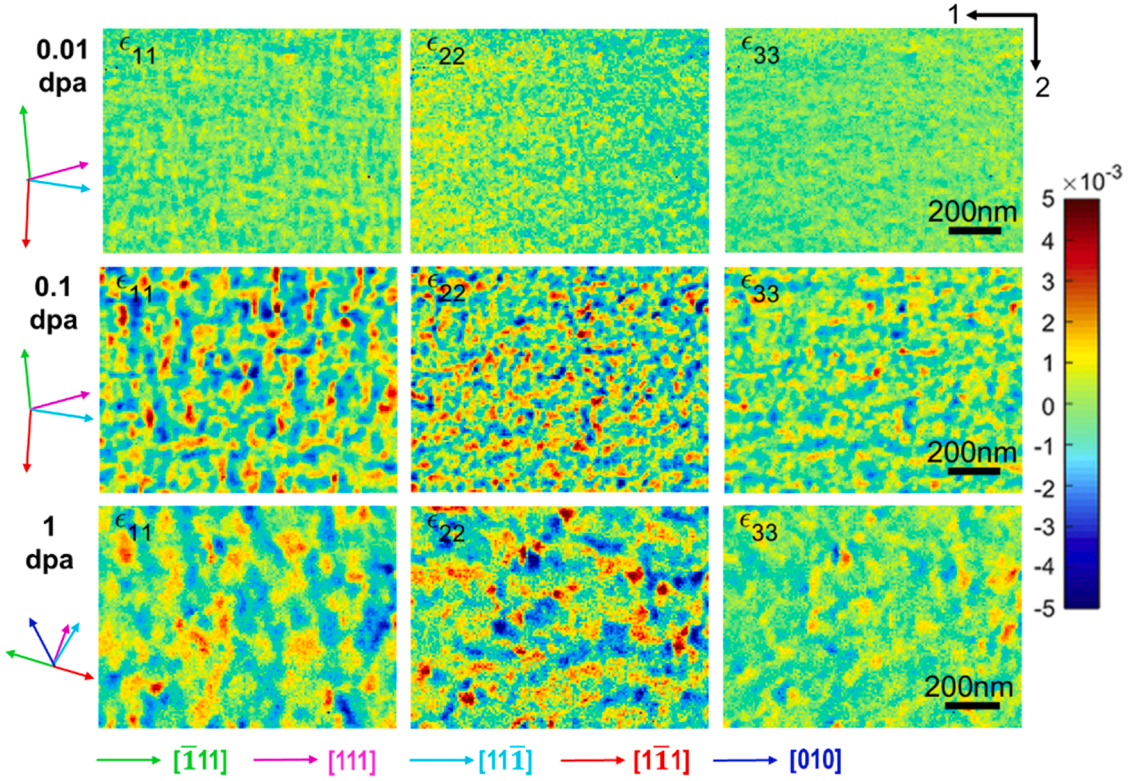

Fig. 3. Evolution of elastic strains (ε) as a function of irradiation dose. The coloured arrows on the left side indicate the directions of different Burgers vectors.

variation of the strain fields, and are normalised such that their mean strain is zero. The assumption of zero out-of-plane stress, commonly used in HR-TKD analysis, was not employed. The results are insensitive to the precise choice of reference pattern, as shown in supplementary section S1 for the 0.1 dpa sample. All strain and rotation components for all dose levels are shown in the supplementary material (Fig. S4 to S6). Fig. 3 shows the evolution of the three direct strain components (ε11, ε22, ε33). The following analysis concentrates on these strain components as they have least experimental uncertainty.

The magnitude of elastic strains in the 0.01 dpa sample is relatively small, but they are still visible even using a colour scale of $[-5, 5] \times 10^{-3}$. The magnitude of the strain fluctuations can be quantitatively represented by the histograms of the deviation from the mean. Fig. 4(a) shows the histograms of the deviation from the mean for the normal strain components. The full-widths-at-half-maximum (FWHMs) of the ε_{11}, ε_{22}, and ε_{33} histograms for the 0.01 dpa sample are approximately 9×10^{-4}, 1.5×10^{-3}, and 7×10^{-4}, respectively. Short-range fluctuation of the lattice strain can be seen in the normal strain components and the ε_{13} shear component at 0.01 dpa. TIFT analysis was used to determine the characteristic length of these short-range fluctuation (Fig. 4(b)), which for the 0.01 dpa sample falls into range of 30 to 50 nm. This also explains why HR-EBSD (spatial resolution > 50 nm) failed to show strain fluctuations at 0.01 dpa in a previous HR-EBSD study on irradiation damage [20].

Strain fluctuations become more obvious in the 0.1 and 1 dpa samples (Fig. 3). This can also be seen in the histograms of the strain deviations from the mean (Fig. 4(a)), where the FWHMs of the 0.1 dpa and 1 dpa samples are significantly greater than of the 0.01 dpa sample. With increasing dose the wavelength of the strain field fluctuations also increases, as clearly seen in the strain maps (Fig. 3) and the TIFT analysis profiles (Fig. 4(b)). The characteristic wavelength of the normal strain fluctuations is 50 - 100 nm at 0.1 dpa and 100 – 200 nm at 1 dpa.

Interestingly, there is a clear spatial ordering of the strain fluctuations at all three damage levels (Fig. 3). At 0.01 and 0.1 dpa, the strain field of the ε_{11} component predominately extends along the ⟨111⟩ directions, which is the energetically most favourable Burgers vector. At 1 dpa, some alignment along the ⟨100⟩ direction (less energetically favourable Burgers vector) is also observed, though alignment along the ⟨111⟩ directions still dominates.

A comparison between TEM observations and strain maps from medium thickness regions as a function of dose reveals an interesting picture: From 0.01 dpa to 0.1 dpa, there is little change in the average size of the individual dislocation loops (from 5.2 nm to 5.3 nm respectively) and the clustering size measured from the TIFT. The prominent observable change is the spatial configuration of dislocation loops, as more rafting structures are seen at 0.1 dpa than at 0.01 dpa (Fig. 1). However, there is a substantial increase in the magnitude of the strain fluctuations and the ordering of strain fluctuations. TKD strain measurements have a spatial resolution of ~ 12 nm [24], as such the probed strain is a convolution of the beam size with the actual strain field. For an isolated small loop, the largest strains are near the core of the loop [31]. Convolution with the electron beam will smear the strain field and give a smaller strain spread over a relatively wider range. Therefore, short-range fluctuations of smaller amplitude were observed in the strain fields of the 0.01 dpa sample – here HR-TKD effectively functions as a low-pass filter for the real strain field. The longer-range, larger amplitude strain fluctuations at 0.1 dpa are presumably due to the spatial ordering of dislocation loops driven by mutual elastic trapping [12]. The elastic trapping of dislocation loops is due to the angular dependence of elastic loop-loop interactions [5,6,11]. Langevin dynamics simulations [12] have shown that loops with collinear Burgers vectors are most strongly bound, which results in the formation of collectively stable raft structures . This is seen in the medium region of the 0.1 dpa sample (Fig. 1). These raft structures presumably result in the formation of longer range collective strain fields, over 50 nm in scale, much larger than the size of individual dislocation loops and the probe resolution.

Elastic strain reflects the elastic energy stored in the lattice. To estimate the real strain energy, measurements of the full lattice tensor are required, inaccessible to HR-TKD. Still, we can obtain the trend of the elastic energy change with damage dose by considering the sum-of-squares of the normal strains. For 0.01, 0.1 and 1 dpa we obtain

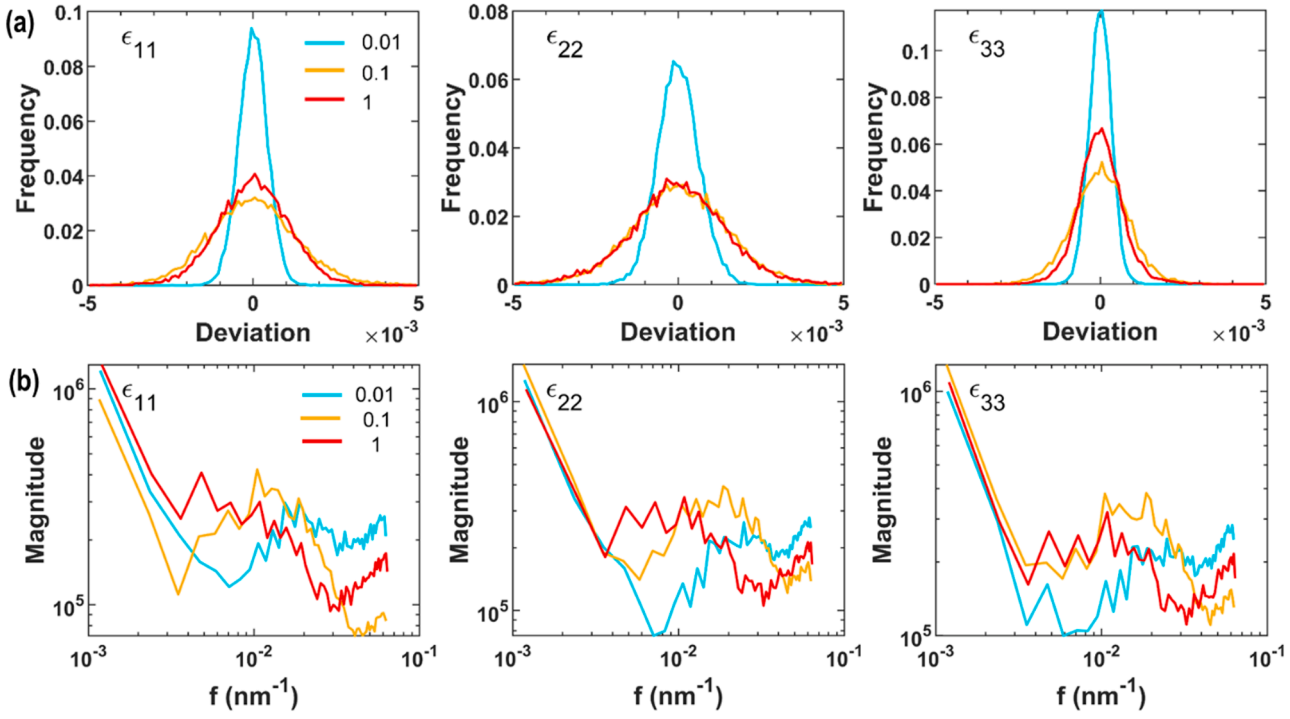

Fig. 4. (a) Histograms of deviation from the mean for the normal strain components. (b) TIFT analysis of the normal strain maps. The colour-coding of line profiles corresponds to the different damage profiles of 0.01, 0.1 and 1 dpa.

0.0107, 0.073 and 0.059 respectively. This suggests a decrease in elastic strain energy from 0.1 dpa to 1 dpa, though the wavelength of strain fluctuations increases. The maximum of elastic energy near 0.1 dpa coincides with the onset of the saturation of irradiation-induced hardening [32] and irradiation-induced thermal diffusivity degradation [33] at ~0.1 dpa in 20 MeV self-ion irradiated pure tungsten. However, the saturation of material properties was less clearly correlated to quantity and morphology of irradiated-induced defects, i.e. the density and size, that are normally studied. This is reasonable, especially for mechanical properties, because it is the interaction of elastic strain fields of irradiation-induced defects with glide dislocations that modify mechanical properties. The decrease in strain energy from 0.1 dpa to 1 dpa may be due to growth of interstitial loops and the formation of new lattice planes by coalescence of interstitials loops [13].

Conclusion

We have used TEM and HR-TKD to study the defect structures in Tungsten irradiated with 2 MeV self-ions to 0.01 dpa, 0.1 dpa and 1 dpa. Foil thickness has a profound effect on the self-organisation of irradiation defects, with free surfaces restricting the self-organisation of defects. Only thicker foils show defect rafting and formation of extended defect structures. The length scale of defect ordering increases with dose, to more than 100 nm at 1 dpa, much greater than individual cascades. HR-TKD reveals extended strain fields associated with this defect self-organisation. Their characteristic length increases with increasing dpa and is consistent with TEM observations. Surprisingly our results suggest a maximum of elastic strain energy near 0.1 dpa, coinciding with the onset of saturation of irradiation-induced property change.

Declaration of Competing Interest

The authors declare that they have no known competing financial interests or personal relationships that could have influenced the work reported in this paper.

Acknowledgements

This research was funded by Leverhulme Trust Research Project Grant RPG-2016–190 and European Research Council Starting Grant 714697. The authors acknowledge the use of characterisation facilities within the David Cockayne Centre for Electron Microscopy, Department of Materials, University of Oxford.

Supplementary materials and data

Supplementary material associated with this article can be found, in the online version, at doi:10.1016/j.scriptamat.2023.115687. Raw data and analysis codes can be found at doi: 10.5281/zenodo.8188933.

References

[1] M.L. Jenkins, Characterisation of radiation-damage microstructures by TEM, J. Nucl. Mater. 216 (1994) 124–156, https://doi.org/10.1016/0022-3115(94)90010-8.
[2] M.L. Jenkins, M.A. Kirk, Characterisation of Radiation Damage By Transmission Electron Microscopy, 1st ed., CRC Press, Boca Raton, 2000 https://doi.org/10.1201/9781420034646.
[3] M.A. Kirk, M. Li, D. Xu, B.D. Wirth, Predicting neutron damage using TEM with in situ ion irradiation and computer modeling, J. Nucl. Mater. 498 (2018) 199–212, https://doi.org/10.1016/j.jnucmat.2017.10.023.
[4] M. Li, M.A. Kirk, P.M. Baldo, D. Xu, B.D. Wirth, Study of defect evolution by TEM with in situ ion irradiation and coordinated modeling, Philos. Mag. 92 (2012) 2048–2078, https://doi.org/10.1080/14786435.2012.662601.
[5] X. Yi, A.E. Sand, D.R. Mason, M.A. Kirk, S.G. Roberts, K. Nordlund, S.L. Dudarev, Direct observation of size scaling and elastic interaction between nano-scale defects in collision cascades, EPL (Europhysics Lett.) 110 (2015) 36001, https://doi.org/10.1209/0295-5075/110/36001.
[6] D.R. Mason, A.E. Sand, X. Yi, S.L. Dudarev, Direct observation of the spatial distribution of primary cascade damage in tungsten, Acta Mater. 144 (2018) 905–917, https://doi.org/10.1016/j.actamat.2017.10.031.
[7] X. Yi, M.L. Jenkins, K. Hattar, P.D. Edmondson, S.G. Roberts, Characterisation of radiation damage in W and W-based alloys from 2MeV self-ion near-bulk implantations, Acta Mater. 92 (2015) 163–177, https://doi.org/10.1016/j.actamat.2015.04.015.
[8] X. Yi, M.L. Jenkins, M.A. Kirk, Z. Zhou, S.G. Roberts, In-situ TEM studies of 150keV W+ ion irradiated W and W-alloys: damage production and microstructural evolution, Acta Mater 112 (2016) 105–120, https://doi.org/10.1016/j.actamat.2016.03.051.
[9] Z. Yao, M. Hernández-Mayoral, M.L. Jenkins, M.A. Kirk, Heavy-ion irradiations of Fe and Fe–Cr model alloys Part 1: damage evolution in thin-foils at lower doses, Philos. Mag. 88 (2008) 2851–2880, https://doi.org/10.1080/14786430802380469.
[10] A. Harte, D. Jädernäs, M. Topping, P. Frankel, C.P. Race, J. Romero, L. Hallstadius, E.C. Darby, M. Preuss, The effect of matrix chemistry on dislocation evolution in an irradiated Zr alloy, Acta Mater 130 (2017) 69–82, https://doi.org/10.1016/j.actamat.2017.03.024.
[11] D.R. Mason, X. Yi, M.A. Kirk, S.L. Dudarev, Elastic trapping of dislocation loops in cascades in ion-irradiated tungsten foils, J. Phys. Condens. Matter. 26 (2014), 375701, https://doi.org/10.1088/0953-8984/26/37/375701.
[12] S.L. Dudarev, K. Arakawa, X. Yi, Z. Yao, M.L. Jenkins, M.R. Gilbert, P.M. Derlet, Spatial ordering of nano-dislocation loops in ion-irradiated materials, J. Nucl. Mater. 455 (2014) 16–20, https://doi.org/10.1016/j.jnucmat.2014.02.032.
[13] D.R. Mason, S. Das, P.M. Derlet, S.L. Dudarev, A.J. London, H. Yu, N.W. Phillips, D. Yang, K. Mizohata, R. Xu, F. Hofmann, Observation of transient and asymptotic driven structural states of tungsten exposed to radiation, Phys. Rev. Lett. 125 (2020), 225503, https://doi.org/10.1103/PhysRevLett.125.225503.
[14] S. Das, W. Liu, R. Xu, F. Hofmann, Helium-implantation-induced lattice strains and defects in tungsten probed by X-ray micro-diffraction, Mater. Des. 160 (2018) 1226–1237, https://doi.org/10.1016/j.matdes.2018.11.001.
[15] F. Hofmann, D. Nguyen-Manh, M.R. Gilbert, C.E. Beck, J.K. Eliason, A.A. Maznev, W. Liu, D.E.J. Armstrong, K.A. Nelson, S.L. Dudarev, Lattice swelling and modulus change in a helium-implanted tungsten alloy: x-ray micro-diffraction, surface acoustic wave measurements, and multiscale modelling, Acta Mater. 89 (2015) 352–363, https://doi.org/10.1016/j.actamat.2015.01.055.
[16] F. Hofmann, E. Tarleton, R.J. Harder, N.W. Phillips, P.W. Ma, J.N. Clark, I. K. Robinson, B. Abbey, W. Liu, C.E. Beck, 3D lattice distortions and defect structures in ion-implanted nano-crystals, Sci. Rep. 7 (2017) 45993, https://doi.org/10.1038/srep45993.
[17] N.W. Phillips, H. Yu, S. Das, D. Yang, K. Mizohata, W. Liu, R. Xu, R.J. Harder, F. Hofmann, Nanoscale lattice strains in self-ion implanted tungsten, Acta Mater. 195 (2020) 219–228, https://doi.org/10.1016/j.actamat.2020.05.033.
[18] F. Hofmann, R.J. Harder, W. Liu, Y. Liu, I.K. Robinson, Y. Zayachuk, Glancing-incidence focussed ion beam milling: a coherent X-ray diffraction study of 3D nano-scale lattice strains and crystal defects, Acta Mater. 154 (2018) 113–123, https://doi.org/10.1016/j.actamat.2018.05.018.
[19] A.J. Wilkinson, G. Meaden, D.J. Dingley, High-resolution elastic strain measurement from electron backscatter diffraction patterns: new levels of sensitivity, Ultramicroscopy 106 (2006) 307–313, https://doi.org/10.1016/j.ultramic.2005.10.001.
[20] H. Yu, P. Karamched, S. Das, J. Liu, K. Mizohata, F. Hofmann, New perspectives on collision cascade damage in self-ion irradiated tungsten from HR-EBSD and ECCI, J. Nucl. Mater. 554 (2021), 153074, https://doi.org/10.1016/j.jnucmat.2021.153074.
[21] J.J. Fundenberger, E. Bouzy, D. Goran, J. Guyon, A. Morawiec, H. Yuan, Transmission Kikuchi Diffraction (TKD)via a horizontally positioned detector, Microsc. Microanal. 21 (2015) 1101–1102, https://doi.org/10.1017/S1431927615006297.
[22] F. Niessen, A. Burrows, A.B. da, S. Fanta, A systematic comparison of on-axis and off-axis transmission Kikuchi diffraction, Ultramicroscopy 186 (2018) 158–170, https://doi.org/10.1016/j.ultramic.2017.12.017.
[23] J.J. Fundenberger, E. Bouzy, D. Goran, J. Guyon, H. Yuan, A. Morawiec, Orientation mapping by transmission-SEM with an on-axis detector, Ultramicroscopy 161 (2016) 17–22, https://doi.org/10.1016/j.ultramic.2015.11.002.
[24] H. Yu, J. Liu, P. Karamched, A.J. Wilkinson, F. Hofmann, Mapping the full lattice strain tensor of a single dislocation by high angular resolution transmission Kikuchi diffraction (HR-TKD), Scr. Mater. 164 (2019) 36–41, https://doi.org/10.1016/j.scriptamat.2018.12.039.
[25] J. Knaster, A. Moeslang, T. Muroga, Materials research for fusion, Nat. Phys. 12 (2016) 424–434, https://doi.org/10.1038/nphys3735.
[26] M. Rieth, S.L. Dudarev, S.M. Gonzalez de Vicente, J. Aktaa, T. Ahlgren, S. Antusch, D.E.J. Armstrong, M. Balden, N. Baluc, M.F. Barthe, W.W. Basuki, M. Battabyal, C. S. Becquart, D. Blagoeva, H. Boldyryeva, J. Brinkmann, M. Celino, L. Ciupinski, J. B. Correia, A. De Backer, C. Domain, E. Gaganidze, C. García-Rosales, J. Gibson, M. R. Gilbert, S. Giusepponi, B. Gludovatz, H. Greuner, K. Heinola, T. Höschen, A. Hoffmann, N. Holstein, F. Koch, W. Krauss, H. Li, S. Lindig, J. Linke, C. Linsmeier, P. López-Ruiz, H. Maier, J. Matejicek, T.P. Mishra, M. Muhammed, A. Muñoz, M. Muzyk, K. Nordlund, D. Nguyen-Manh, J. Opschoor, N. Ordás, T. Palacios, G. Pintsuk, R. Pippan, J. Reiser, J. Riesch, S.G. Roberts, L. Romaner, M. Rosiński, M. Sanchez, W. Schulmeyer, H. Traxler, A. Ureña, J.G. van der Laan, L. Veleva, S. Wahlberg, M. Walter, T. Weber, T. Weitkamp, S. Wurster, M.A. Yar, J. H. You, A. Zivelonghi, Recent progress in research on tungsten materials for

nuclear fusion applications in Europe, J. Nucl. Mater. 432 (2013) 482–500, https://doi.org/10.1016/j.jnucmat.2012.08.018.
[27] J.F. Ziegler, M.D. Ziegler, J.P. Biersack, SRIM – The stopping and range of ions in matter (2010), Nucl. Instruments Methods Phys. Res. Sect. B Beam Interact. Mater. Atoms. 268 (2010) 1818–1823, https://doi.org/10.1016/j.nimb.2010.02.091.
[28] J. Liu, S. Lozano-Perez, A.J. Wilkinson, C.R.M. Grovenor, On the depth resolution of transmission Kikuchi diffraction (TKD) analysis, Ultramicroscopy 205 (2019) 5–12, https://doi.org/10.1016/j.ultramic.2019.06.003.
[29] T. Fujita, M.W. Chen, Characteristic length scale of bicontinuous nanoporous structure by fast Fourier transform, Jpn. J. Appl. Phys. 47 (2008) 1161–1163, https://doi.org/10.1143/JJAP.47.1161/XML.
[30] J. Fikar, R. Gröger, R. Schäublin, Interaction of irradiation-induced prismatic dislocation loops with free surfaces in tungsten, Nucl. Instruments Methods Phys. Res. Sect. B Beam Interact. Mater. Atoms. 393 (2017) 186–189, https://doi.org/10.1016/j.nimb.2016.10.006.
[31] Y. Gao, B.C. Larson, Displacement fields and self-energies of circular and polygonal dislocation loops in homogeneous and layered anisotropic solids, J. Mech. Phys. Solids. 83 (2015) 104–128, https://doi.org/10.1016/j.jmps.2015.06.008.
[32] S. Das, H. Yu, K. Mizohata, E. Tarleton, F. Hofmann, Modified deformation behaviour of self-ion irradiated tungsten: a combined nano-indentation, HR-EBSD and crystal plasticity study, Int. J. Plast. 135 (2020), 102817, https://doi.org/10.1016/j.ijplas.2020.102817.
[33] A. Reza, H. Yu, K. Mizohata, F. Hofmann, Thermal diffusivity degradation and point defect density in self-ion implanted tungsten, Acta Mater. 193 (2020) 270–279, https://doi.org/10.1016/j.actamat.2020.03.034.